BRNO UNIVERSITY OF TECHNOLOGY
VYSOKÉ UČENÍ TECHNICKÉ V BRNĚ

FACULTY OF MECHANICAL ENGINEERING
FAKULTA STROJNÍHO INŽENÝRSTVÍ

ENERGY INSTITUTE
ENERGETICKÝ ÚSTAV

REDUCED-ORDER MODEL OF SWIRLING FLOW
REDUKOVANÝ MODEL VÍROVÉHO PROUDĚNÍ

SHORT VERSION OF DOCTORAL THESIS
ZKRÁCENÁ VERZE DIZERTAČNÍ PRÁCE

AUTHOR   Ing. ONDŘEJ URBAN
AUTOR PRÁCE

SUPERVISOR   doc. Ing. PAVEL RUDOLF, Ph.D.
ŠKOLITEL

BRNO 2022

Key words

vortex rope, CFD, swirl generator, dynamic decomposition, reduced-order model

Klíčová slova

vírový cop, CFD, vírový generátor, dynamická dekompozice, redukovaný model

Místo uložení práce

Vysoké učení technické v Brně
Fakulta strojního inženýrství
Technická 2896/2
616 69 Brno

Contents

Introduction

Water turbines are machines designed specifically for given operating conditions. When operating in off-design conditions, the flow is often strongly unsteady and exhibits onset and propagation of pressure pulsations, noise, and vibrations that can negatively affect the lifetime of exposed parts. Such dangerous phenomena often lead to a restriction of the turbine operating range. Let us focus on the draft tube of reaction water turbines, where a helical structure called the vortex rope emerges in a certain range of operating conditions, typically in part load, i.e. when the flow rate is below the design value. The vortex rope is observed when swirl is admitted into the draft tube, and its interaction with the draft tube elbow was found to be the source of significant pressure pulsations. This is a problem specifically in Francis turbines due to their fixed blades. In contrast, Kaplan turbines feature adjustable blades that allow for reduction of the swirl at the runner outlet/draft tube inlet in off-design conditions by changing their pitch angle.

Meanwhile, people are striving to increase the share of renewable energy in the energy mix. This goal can be accomplished by solar and wind power plants. Their output is strongly affected by the weather and therefore very unstable. To ensure stability of the electrical grid, sufficient backup capable of on-demand connection to the grid, output power adjustments, and disconnection from the grid is needed. Water turbines are its key part as they can provide the mentioned actions most rapidly. Naturally, reaching the widest possible operating range has recently become one of the most important demands on new or refurbished machines. This leads to the need for mitigation of the dynamic load caused by unsteady vortical structures.

The presented facts motivate research of the vortex rope phenomenon. The goal of this thesis is to contribute to this research and in particular to extend the work that has been done at the department. The following milestones were pursued.

- *Design of a new swirl generator allowing control of swirl intensity while being inexpensive and easy to manufacture (i.e. no moving parts, bearings, etc.).*

- *Performing CFD simulations of flow in the proposed swirl generator, validating them against the results of PIV measurements, and studying the behavior of the vortex rope and its dependence on operating conditions.*

- *Finding suitable vortex identification methods and proposing visualization techniques leveraging the content of the CFD data.*

- *Conceptual study of several passive and active flow control methods for mitigating the vortex rope.*

- *Reduced-order modelling of the present flow with a vortex rope.*

1 Design of a new swirl generator

The first goal of this work is to design a new swirl generator. The primary requirement is the ability to operate in a wide range of swirl numbers while still being easy to manufacture and relatively cheap, i.e. without moving parts, bearings, etc.

The idea used here is to include a second inlet pipe ended by a spiral case generating the tangential velocity. Having two inlets allows setting a wide range of swirl numbers. The resultant flow coming to the diffuser is given by mixing the two inlet flows – the first is purely axial, the second has a tangential component generated by the spiral case. It follows that increasing the ratio of the tangential to axial inlet flow rates increases the swirl number. A drawback of this method is the nonuniformity and unsteadiness of the resultant flow. The mixing of two different flows is typically accompanied by vortices as a consequence of the Kelvin–Helmholtz instability. Insertion of a ring with fixed guide vanes is considered for future work. A sketch of the new swirl generator with all dimensions and the coordinate system used throughout this work is presented in Fig. 1.1. The final construction design is rendered in Fig. 1.2.
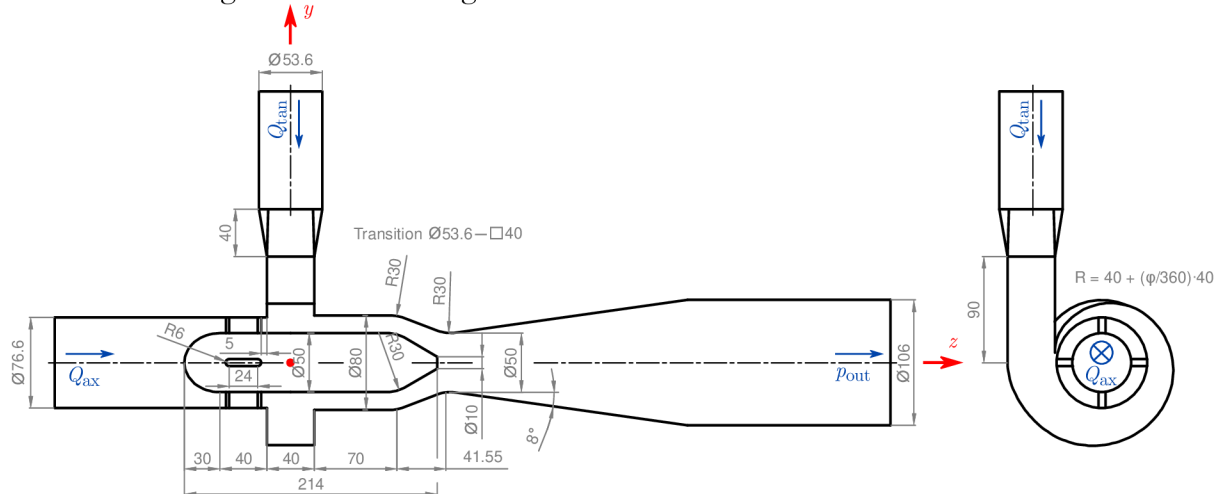

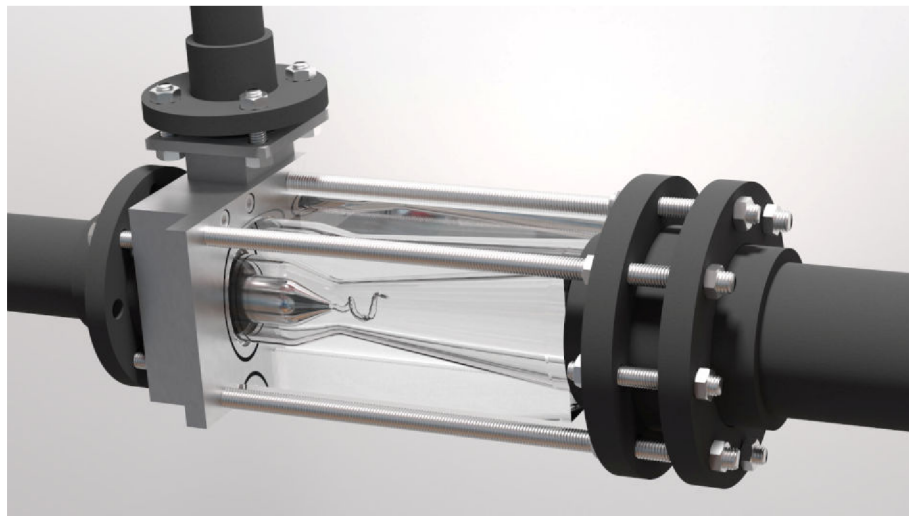**Fig. 1.1:** *A sketch of the new swirl generator.*

Fig. 1.2: *A render of the final construction design with a vortex rope predicted by a CFD simulation with SBES turbulence model.*

2 CFD simulations

2.1 Basic info

The conducted CFD simulations comprise both modelling based on the unsteady Reynolds-averaged Navier–Stokes (URANS) equation and scale-resolving simulations. The URANS computations were carried out during the design phase of the swirl generator, while the scale-resolving calculations were performed afterwards to gain more precise results. The SBES turbulence model was chosen based on the results by Junginger[1]. Simulations were performed in commercial software Fluent version 18.1.

The material properties are common for all the simulations and correspond to water at atmospheric pressure and room temperature. Further on, the results from SBES simulations will mostly be used. Their final setup was the following: WALE model of the subgrid-scale effects (Wall-Adapting Local Eddy-viscosity model), bounded central differencing for the discretization of momentum, PRESTO! (PREssure STaggering Option) scheme for pressure, PISO (Pressure-Implicit with Splitting of Operators) method for pressure-velocity coupling, least squares cell-based for gradients, second order upwind scheme for turbulence quantities, and bounded second order implicit scheme for temporal discretization. The mesh consisted of slightly over 7 million elements. A longitudinal slice through the mesh in the diffuser is presented in Fig. 2.1.
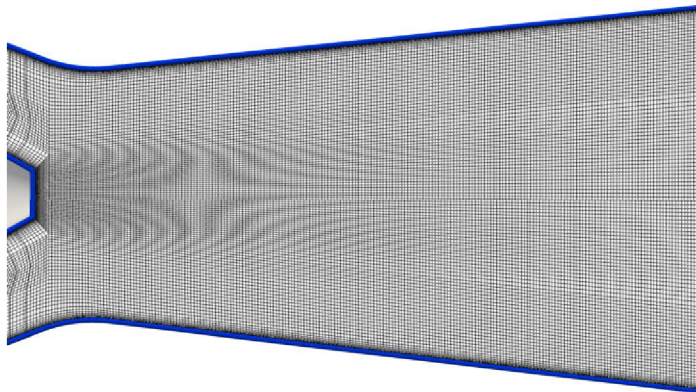

Fig. 2.1: *A longitudinal slice through the mesh for scale-resolving simulations.*

For each simulation, an abbreviation will be used. The first element is an abbreviation of the turbulence model (e.g. RSM, SBES), the second distinguishes between fixed and transient boundary conditions (F for fixed, T for transient). For fixed boundary conditions, the last three elements represent the total flow rate in liters per second and the percentage of the total flow rate at the tangential inlet and the axial inlet, respectively. For transient boundary conditions, there is only a single number to distinguish among the simulations as the boundary conditions are not so easy to express.

2.2 Methodology of CFD data postprocessing

At the end of CFD calculations, we end up with a large amount of spatio-temporal data. To leverage their content, it is necessary to convert them into meaningful representations that can be processed

and understood by the human brain, i.e. to visualize them. This section describes what is in this work visualized and how, in order to get a good notion of the vortex rope dynamics and other flow features. The results presented here have already been published in a journal paper[2] and the bachelor's theses of Častulíková[3] and Kurková[4].

2.2.1 Data visualization techniques

Most of the visualizations in this work were created by volume rendering. It is based on a fictitious light particle moving through the data field. Physically-based phenomena, such as emission, scattering, and absorption, can be considered[5]. Their parameters are given by the data values, i.e. we map the data values to a parameter (e.g. the emission strength) using a defined transfer function. In the end, we obtain a 2D field to be displayed on the screen. The development of this technique is driven particularly by medicine with applications to computed tomography (CT) or magnetic resonance imaging (MRI) data[6]. The art of volume rendering resides in the selection of the emission, scattering, and absorption parameters, where it is advisable to make unimportant parts of the data domain completely transparent and find such settings for the rest that provide the best notion of how the scalar values are distributed in the 3D space.

   To the author's knowledge, volume rendering is used only seldom in the field of hydraulic machinery. Considering its advantages over dominantly used isosurfaces and its availability in software, it seems to the author as an oversight, especially with regard to the growing numbers of detailed simulations (scale-resolving turbulence models, LES) that capture a rich spectrum of structures. Visualizations with only a single isosurface are similar to a map with only a single elevation contour line. It is possible to determine where a peak might be located in the terrain, but no information is given on its elevation and shape. Similarly, visualizations using only a single isosurface provide no information on what the field looks like both inside and outside of it. A well-made volume render can, in contrast, provide a good notion of the whole visualized scalar field.

   A drawback of volume rendering that should be mentioned is that it is slow on unstructured grids. This is usually overcome by interpolating the data to a structured grid. One issue is with significant local refinements as the structured grid has all cells of the same size. Another issue arises if curved boundaries need to be captured. After the interpolation to a structured grid, they become jagged. Considering that the mentioned issues are not relevant in this work, volume rendering was chosen as the primary method of scalar fields visualization.

2.2.2 Dimensionless quantities

For comparability of results among different cases, quantities are often nondimensionalized, i.e. scaled relative to a reference value. In this work, velocity and pressure are nondimensionalized. The reference value of velocity is the mean velocity in the throat

$$\hat{\boldsymbol{v}} = \frac{\boldsymbol{v}}{v_{\text{ref}}}, \qquad v_{\text{ref}} = \frac{Q_{\text{total}}}{S_{\text{throat}}} = \frac{4Q_{\text{total}}}{\pi d_{\text{throat}}{}^2} \tag{2.1}$$

where $d_{\text{throat}} = 50$ mm (see Fig. 1.1), and the reference value of pressure is the dynamic pressure exerted by the reference velocity

$$\hat{p} = \frac{p}{p_{\text{ref}}} = \frac{p}{\frac{1}{2}\rho v_{\text{ref}}{}^2} = \frac{p\pi^2 d_{\text{throat}}{}^4}{8\rho Q_{\text{total}}{}^2} \tag{2.2}$$

2.2.3 Vortex identification

The central task of vortex rope visualizations is to identify the vortex rope itself. The simplest way is to exploit the fact that static pressure decreases towards the vortex rope core. Another way is to use various vortex identification methods. Although the intuitive notion of a vortex as a portion of fluid rotating around a common axis (vortex core) is clear, there is no widely accepted rigorous definition capable of clearly distinguishing the vortices among other possible flow structures. Kolář[7] presented a review of the most popular vortex identification methods and summarized the requirements on vortex definitions. The problem resides in the inability of the methods to meet all the requirements and in the arguability of some of them. In the following, the method of choice in this work, the residual vorticity, will be described.

Residual vorticity

This more elaborate vortex criterion was proposed by Kolář[7]. It tackles the drawback of vorticity, i.e. admitting nonzero values not only for purely rotating flows but also for purely shearing flows. The proposed method is based on a triple decomposition of the velocity gradient into so-called effective shear, residual strain, and residual rotation parts. The last part leads to the residual vorticity, i.e. a portion of the original vorticity related only to shearless motion. A bottleneck of this method is the effective shear extraction procedure. First, the decomposition of the velocity gradient tensor is defined as follows

$$\nabla \boldsymbol{v} = \nabla \boldsymbol{v}_{\text{shear}} + \nabla \boldsymbol{v}_{\text{residual}} \tag{2.3}$$

$$\nabla \boldsymbol{v}_{\text{residual}} = \boldsymbol{\Upsilon}, \qquad \Upsilon_{ij} = \left(\operatorname{sgn}\frac{\partial v_i}{\partial x_j}\right)\min\left(\left|\frac{\partial v_i}{\partial x_j}\right|, \left|\frac{\partial v_j}{\partial x_i}\right|\right) \tag{2.4}$$

The shear tensor is by definition purely asymmetric, and this procedure is proposed so that this property is satisfied. The results, however, depend on the choice of the frame of reference. We seek the frame in which the Frobenius norm of the residual tensor is minimized. The shear part in this so-called best reference frame (BRF) is denoted as the effective shear. Kolář also derived a relation between $\|\nabla \boldsymbol{v}\|$ and $\|\nabla \boldsymbol{v}_{\text{residual}}\|$

$$\|\nabla \boldsymbol{v}_{\text{residual}}\|^2 + 4(|S_{12}R_{12}| + |S_{23}R_{23}| + |S_{31}R_{31}|) = \|\nabla \boldsymbol{v}\|^2 \tag{2.5}$$

Considering the fact that $\|\nabla \boldsymbol{v}\|$ remains unchanged in all frames, the BRF is defined as the frame where $|S_{12}R_{12}| + |S_{23}R_{23}| + |S_{31}R_{31}|$ is maximized. The computation of the residual vorticity therefore involves time-consuming optimization. Once the BRF is found, the residual tensor is computed, and then the residual vorticity is extracted from its antisymmetric part and returned back to the original frame. As this criterion is currently not available in both Ansys and ParaView softwares (probably due to the long-lasting calculations), a custom Python programmable filter for ParaView was created.

An advantage of vorticity-based criteria is that the vorticity also determines the swirl orientation. Axial vorticity can be used to determine the sense of rotation of the vortex rope. A modified residual vorticity is for this purpose proposed as follows

$$\widetilde{\Omega}_{\text{residual}} = \|\boldsymbol{\Omega}_{\text{residual}}\| \operatorname{sgn} \Omega_{\text{residual}_z} \tag{2.6}$$

This is a scalar quantity, and its field can therefore be visualized by volume rendering. The sign of this quantity corresponds to the sign of the axial residual vorticity and distinguishes between clockwise and counterclockwise rotation of the respective elementary particle around the axis parallel to the diffuser axis. Its magnitude corresponds to the residual vorticity magnitude and serves as a measure of the swirl intensity.

2.3 Comparison of CFD results with PIV measurements

The new swirl generator designed in this work was the subject of PIV measurements carried out in cooperation with Institute of Thermomechanics of the Czech Academy of Sciences as part of a research project. The main purpose is to compare the measurements with the results of CFD simulations to find out whether the CFD can reasonably predict the flow and consequently whether it is worth studying the results more in detail.

For comparison of the CFD results with the measurements, three outcomes will be used: mean velocity fields, mean turbulence kinetic energy field, and discrete Fourier transform of axial velocity.

Looking at the mean velocity fields presented in Fig. 2.2, the results of PIV and CFD SBES are very similar except for discrepancies that can be explained by positional inaccuracies. Different radial velocity fields in the upper part indicate that the measured plane could have a certain offset. Leaving aside these discrepancies, it can be stated that the mean velocity fields are well predicted by the SBES simulations and slightly worse by the RSM simulation. The turbulence kinetic energy is also well predicted by the SBES simulations. The RSM simulation resulted in lower values, which is expected as this turbulence model does not resolve any eddies.

The discrete Fourier spectra of the PIV measurements and the SBES simulation are also similar. There are two low-frequency peaks and then the most dominant peak around 30 Hz. It is noted that the spectra largely depend on the time interval covered by the data. The PIV covers in both cases more than 3 seconds, which is much more than both CFD simulations. For this reason, the PIV data were split into several parts that cover the same time as the SBES simulations. The obtained spectra for each part were averaged, and the RMS value of the fluctuations was computed.

As the last point, results of CFD simulations with the SBES turbulence model are compared in Fig. 2.3 with high-speed camera recordings to assess whether the vortex rope shape and behavior are well predicted by the simulations. For both operating points, the behavior of the vortex rope is similar and it is possible to find matching situations.

In the first case, a thin vortex rope is observed. It is shown in the middle picture that the vortex filament may twist and form a vortex ring. The right picture illustrates that the filament may also break into two intertwined vortices, which happens most often right under the hub tip. In the second case, we observe a complex behavior of vortical structures under the hub tip. The three pictures illustrate that the number of vortices changes over time. We can observe either a single vortex or mostly twin vortex ropes, which may also break into a larger number of smaller vortices.

Overall, it is concluded that the results of the simulations are worth further study, which is the subject of the following section.
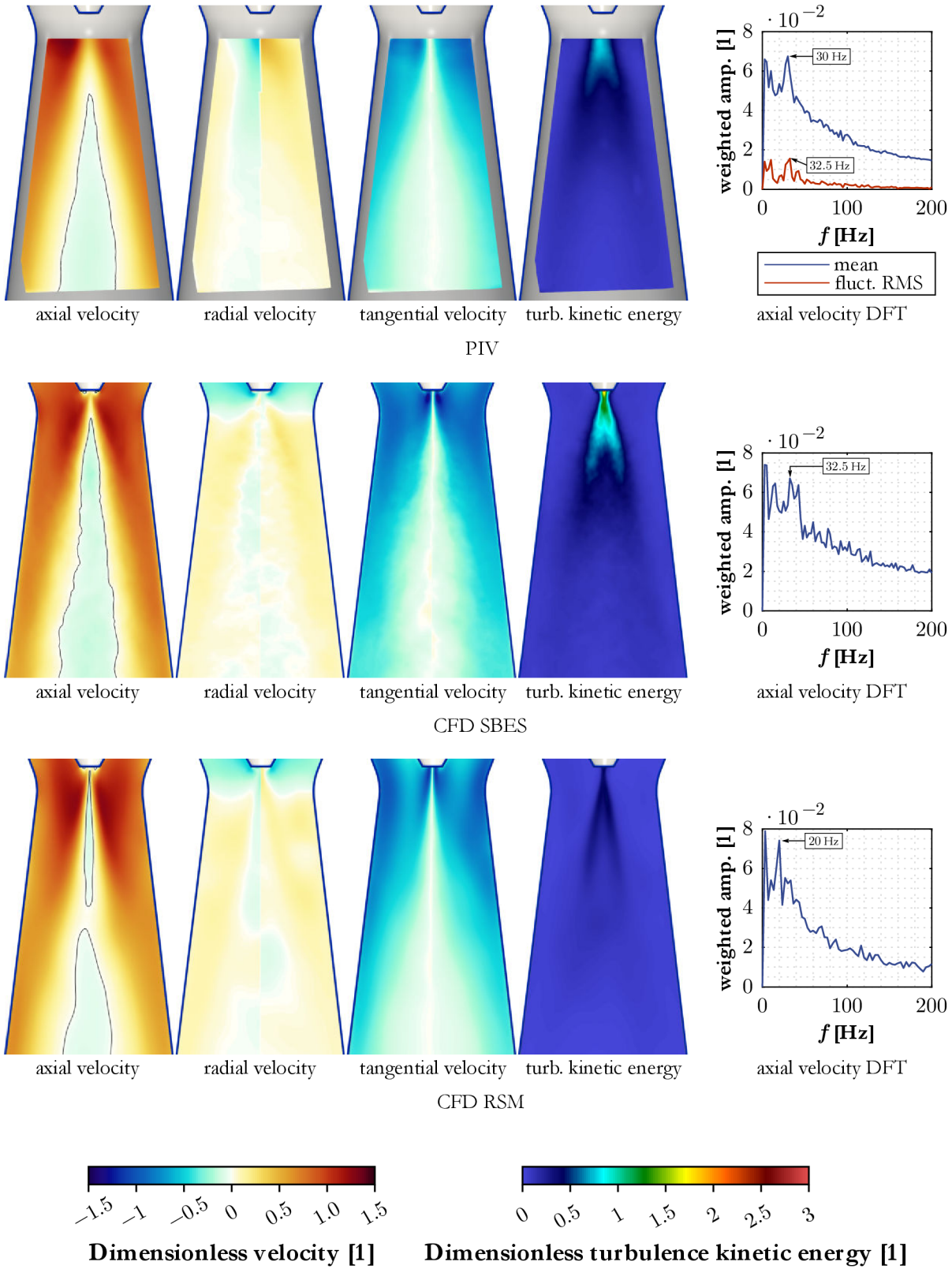
Fig. 2.2: *Results of PIV measurements and CFD simulations with the SBES and RSM turbulence models. Operating point with a flow rates ratio of 50:50 and a total flow rate of 10 l/s. The black line in the axial velocity field is the contour of zero value.*
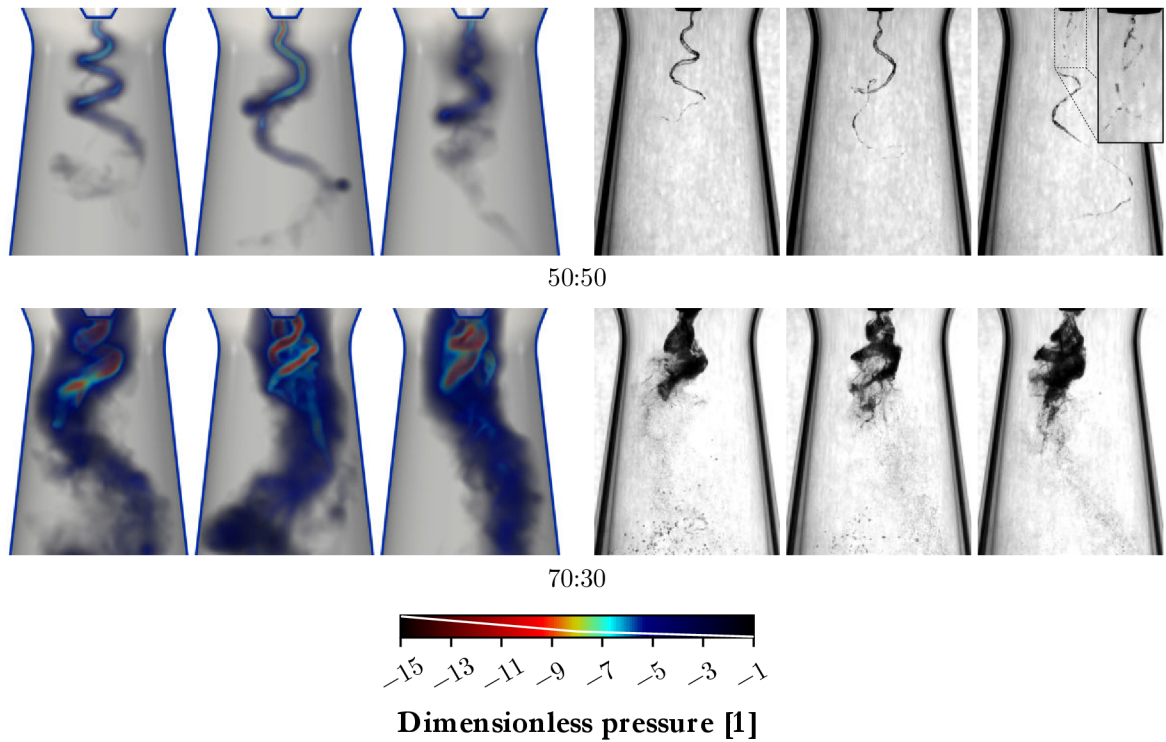
Fig. 2.3: *Results from CFD simulations with the SBES turbulence model (left) and high-speed camera recordings (right). Operating points with flow rates ratios of 50:50 and 70:30.*
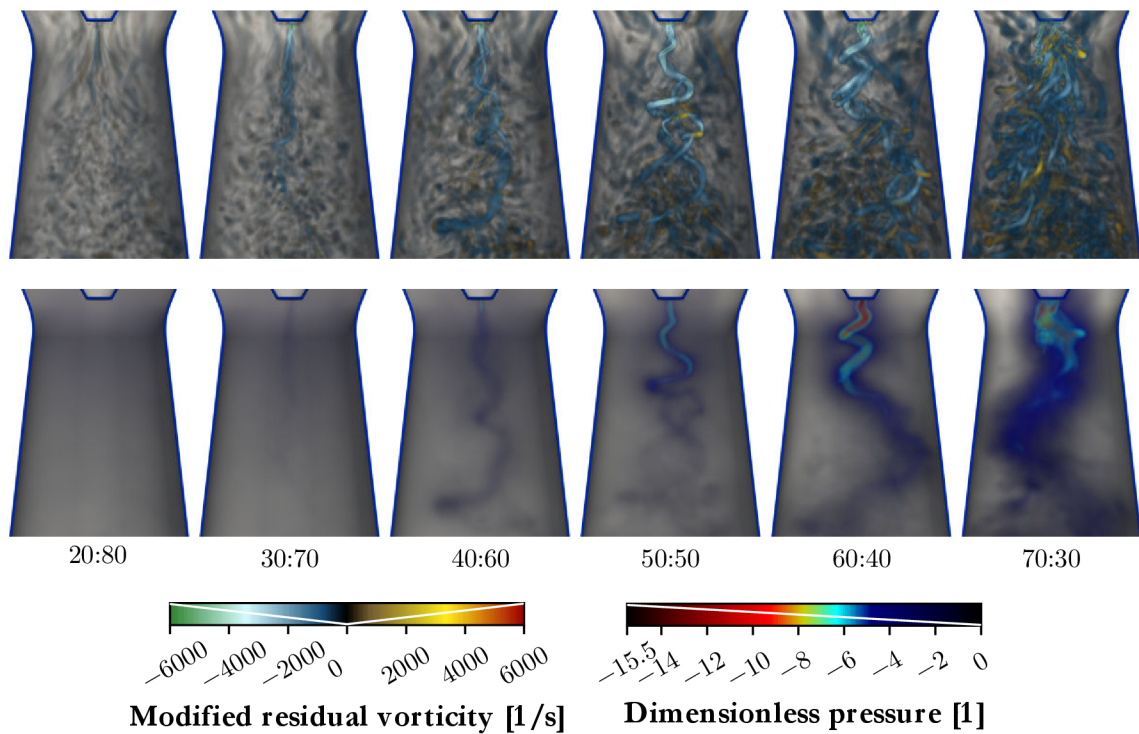

Fig. 2.4: *Evolution of the modified residual vorticity (top) and dimensionless pressure (bottom) as the boundary conditions change. The flow rates ratios are listed below each pair of pictures.*

2.4 Results of simulations

2.4.1 Visualizations of the vortex rope for different flow rates ratios

The vortex rope is most often visualized using static pressure. This quantity is important in practice as it indicates the possibility of cavitation, and its values are typically measured by transducers on the walls to investigate the dynamical behavior of the flow. For identification and visualization of vortical structures, the modified residual vorticity is used.

Fig. 2.4 depicts volume renders of the dimensionless pressure and modified residual vorticity fields in selected time instants from SBES simulations with transient boundary conditions. These snapshots were selected so that the flow rates ratio corresponds to the values listed below the pictures. They document the evolution of the vortex rope as the tangential flow rate increases and the axial flow rate decreases to keep the total flow rate constant. More on the dynamics of the vortex rope is to follow in further sections.

2.4.2 Deceleration at the diffuser axis

The key characteristics of vortex breakdown are a stagnation point and a region of decelerated flow or even backflow further downstream. In Fig. 2.5, it can be seen that the backflow (in terms of average values) at first appears at the end of the diffuser and propagates upstream as the swirl intensity is increased. This is in contrast to the vortex rope, which originates at the hub tip and propagates further downstream. For this reason, the difference between the current axial velocity and the area-weighted axial velocity average is used. The dimensionless axial velocity deficit is defined as follows

$$\hat{v}_{z_{\text{def}}} = \frac{\text{awa}\, v_z - v_z}{v_{\text{ref}}}, \qquad \text{awa}\, v_z = \frac{Q_{\text{total}}}{S} \tag{2.7}$$

where S is the area of the slice that is perpendicular to the diffuser axis and contains the point of interest. This dimensionless axial velocity deficit was evaluated for the SBES simulations with transient boundary conditions and averaged over $T = 0.08$ s.

In the first picture, for the lowest tangential flow rate, we see that a significant deceleration is present only in the wake behind the hub tip. In the second picture, the contours indicate a slight deceleration at the axis. The wake recirculation area is now significantly reduced, especially in the center, which suggests that the emerging vortex rope dominates over the wake effects. In the following pictures, the axial velocity deficit at the axis grows and the area of its positive values gets wider and extends downstream.

20:80
30:70
40:60

50:50
60:40
70:30

Dimensionless v_z average [1]
Dimensionless v_z deficit average [1]
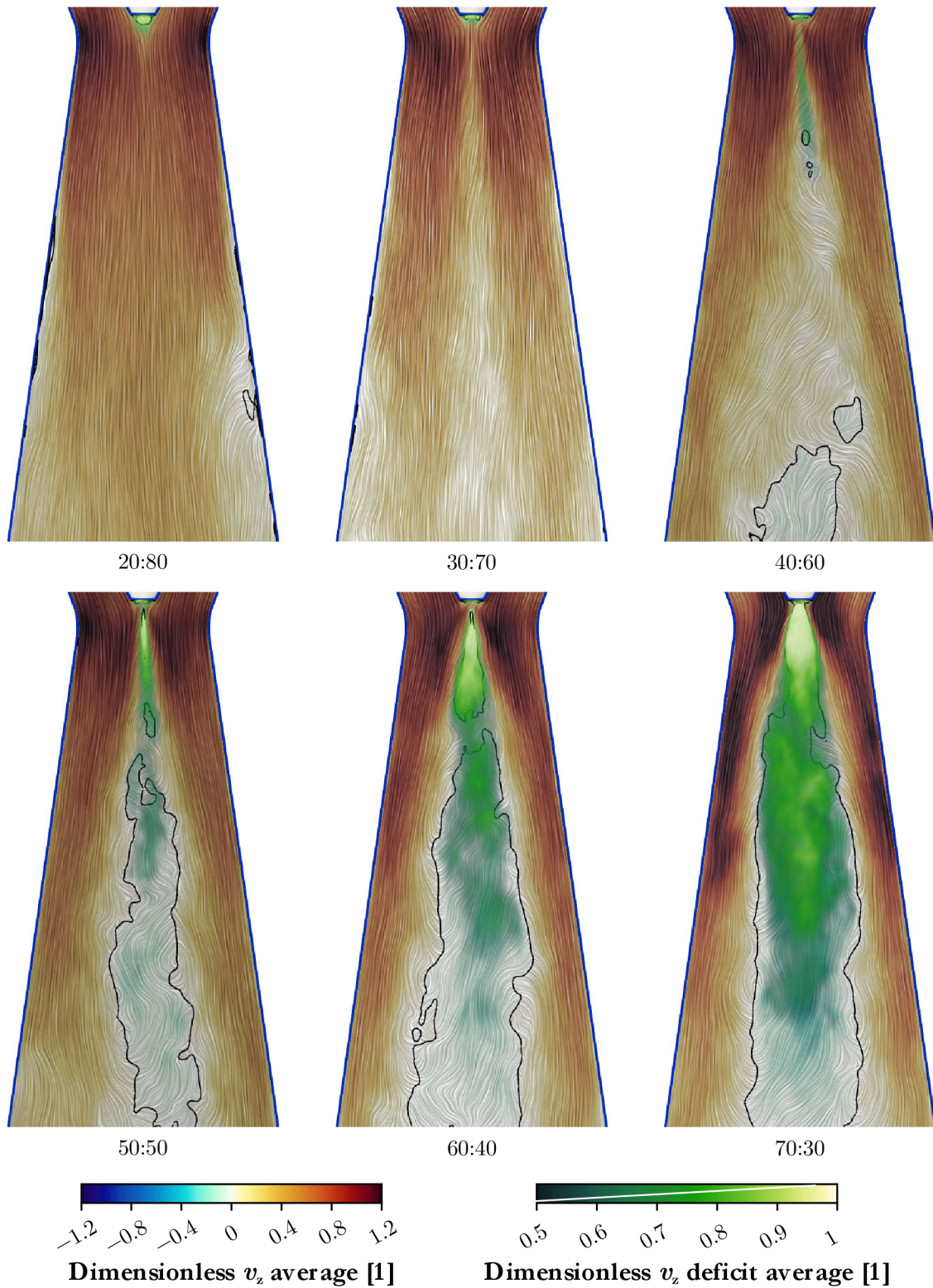
Fig. 2.5: *Volume renders of the dimensionless axial velocity deficit average complemented by contours of the dimensionless axial velocity average, an LIC texture, and the contour of zero axial velocity average (black line) in a longitudinal slice. The quantities are temporally averaged over $T = 0.08$ s. The tangential to axial flow rate ratios are listed below each picture.*

3 A brief study of vortex rope mitigation methods

3.1 CFD study of water jet injection through the hub tip

In this part, the water jet injection method will be tested numerically for the present swirl generator. To make things more interesting, the original straight diffuser was replaced for an elbow one. It corresponds to the draft tube used in Střekov power plant located on the Elbe river in the Czech Republic. The reason for using an elbow diffuser is that synchronous pressure pulsations at the vortex rope precession frequency are not present in straight draft tubes, they were observed only in elbow draft tubes. The resultant flow is therefore expected to feature these synchronous pulsations. Moreover, elbow draft tubes are for practical reasons standardly used in water turbines, so the present case better represents the situation we can encounter in practice. The resultant geometry is depicted in Fig. 3.1.
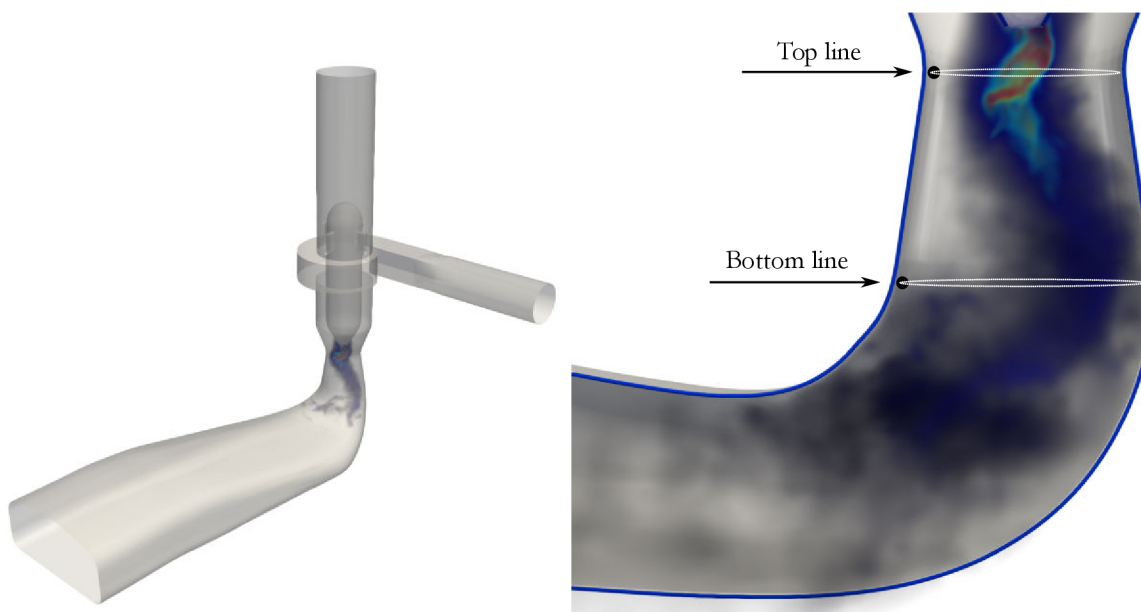

Fig. 3.1: *Left: present swirl generator with an elbow diffuser corresponding to the draft tube used in Střekov power plant. Right: a detail on the upstream part of the diffuser with designated lines where synchronous pressure pulsations were evaluated and points where the asynchronous component was computed.*

A simulation for the flow rates ratio of 70:30 with water jet injection through the whole hub tip surface was carried out. The water jet flow rate increases linearly in time from 0% to 20% of the flow rate coming to the diffuser (5 l/s) during 1.6 s. With the vortex rope precession frequency of 28 Hz, this time interval covers almost 45 precession periods. The scale-resolving SBES model was employed with the same settings as in the previously described simulations.

To check the mentioned presence of synchronous pressure pulsations, data from two lines depicted in Fig. 3.1 were collected. The synchronous component is then defined as the mean value along the line and the asynchronous component as the actual value minus the synchronous component.

In Fig. 3.2, instantaneous snapshots from the simulation of water jet injection are presented. From the axial velocity fields, it is evident that the jet axial velocity is well aligned with the outer

flow for $Q_{\text{jet}}/Q_{\text{total}}$ laying somewhere between 5 and 10%. The reach of the jet is, unfortunately, rather short. Backflow region is still present farther downstream and a spiral vortex is still observed. Increasing the jet flow rate further on extends its reach, but it does not suppress the backflow; instead, the jet is deflected to the side and rotates around the backflow zone in the center. As it can be seen in Fig. 3.3, the frequency of pressure pulsations is slightly lower than in the case without any injection. A very undesirable effect is that the synchronous pulsations are significantly stronger. Overall, the water jet injection as it was proposed in this case actually worsened the situation.
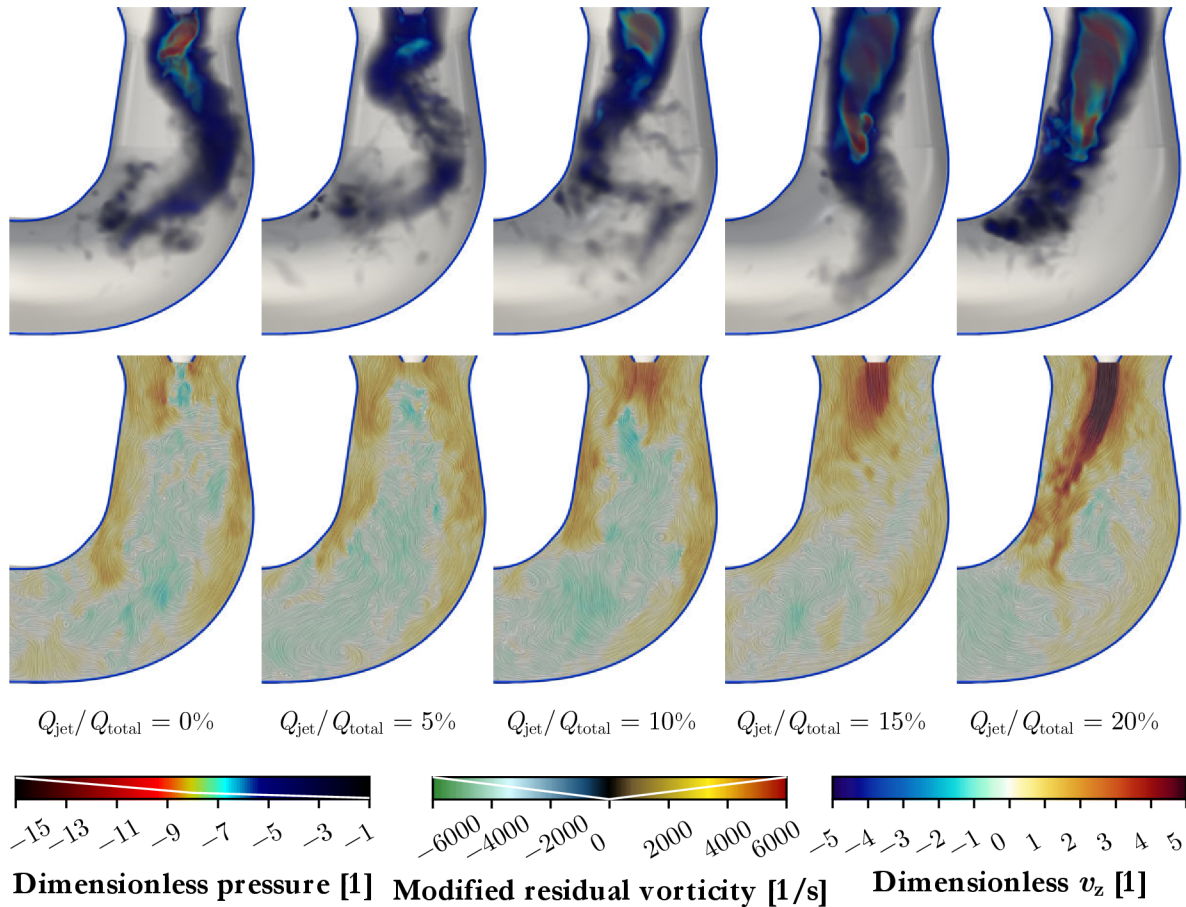
Fig. 3.2: *Instantaneous snapshots from CFD simulation as the water jet flow rate increases.*

The unsatisfactory results obtained so far lead to the need for exploring more configurations. For that reason, a ring on the hub is introduced in Fig. 3.4. This ring will be used as an additional surface for water jet injection. Moreover, it was decided to use the RSM model of turbulence and consider the diffuser only. The inlet was set just behind the spiral case, and profiles of the velocity inlet boundary condition variables were computed in a separate simulation of the whole geometry. Mean values over time were used, i.e. the unsteadiness of the flow therein was neglected. These simplifications led to a substantial reduction of computational burden.

Top line

Bottom line

——— asynchronous pulsations in designated point ——— synchronous pulsations (circumferential average)

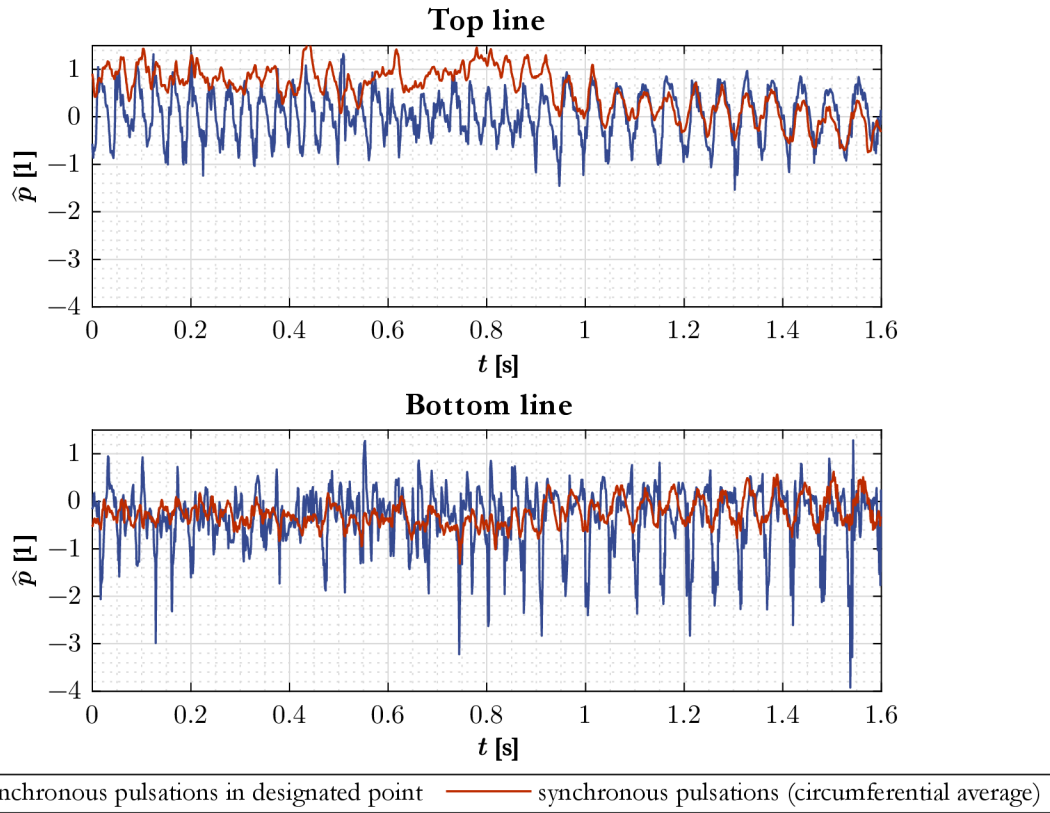**Fig. 3.3:** *Dimensionless pressure evolution in time: synchronous pulsations computed by averaging along lines designated in Fig. 3.1 and asynchronous pulsations for the designated points. Data from the CFD simulation of water jet injection with the jet flow rate increasing linearly in time from 0% to 20% of the total flow rate.*
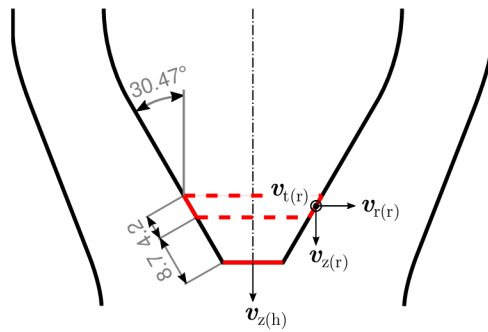
Fig. 3.4: *Geometry of a ring for additional water jet injection. The velocity components that were considered in simulations are also designated.*

As the first step, it was neccessary to ensure that the assumed simplifications do not affect the key characteristics of the flow in the diffuser. The first two simulations therefore considered no control and the water jet injection through the hub tip only, respectively. Four new configurations were tested subsequently. In all the cases, the water jet flow rate was fixed at 20% of the total flow rate. The best turned out to be the second case, which considered water jet injection through the ring and the hub tip simultaneously. The water jet is wider and slower. It moved the stagnation point to the end of the straight conical part. It is likely thanks to the larger cross section of the jet that it remained straight and no deflection and rotation around the backflow zone was observed.

$\widehat{v}_{z(h)} = 5$ $\widehat{v}_{z(r)} = 2.8$ $\widehat{v}_{z(h)} = 1.8$ $\widehat{v}_{z(h)} = 1.8$ $\widehat{v}_{z(h)} = 1.58$

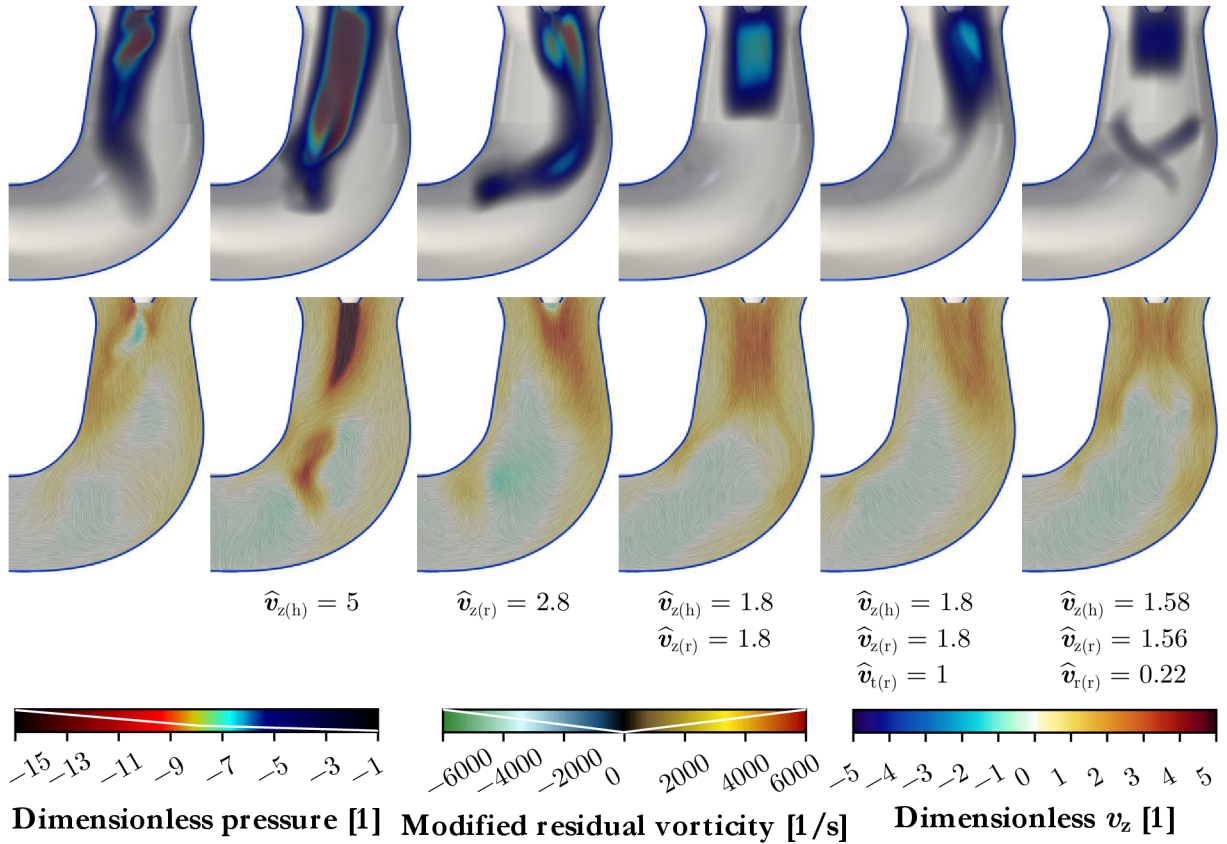$\widehat{v}_{z(r)} = 1.8$ $\widehat{v}_{z(r)} = 1.8$ $\widehat{v}_{z(r)} = 1.56$

$\widehat{v}_{t(r)} = 1$ $\widehat{v}_{r(r)} = 0.22$

Dimensionless pressure [1]   **Modified residual vorticity [1/s]**   **Dimensionless v_z [1]**

Fig. 3.5: *Instantaneous snapshots from CFD simulations with the RSM model of turbulence. The far left case is without control, others are with active flow control by water jet injection with various parameters specified below the pictures.*

3.2 CFD study of different pasive control methods

Several passive control methods for mitigation of the vortex rope were proposed and tested. An exhaustive research report[8] has been written, where details can be found.

The swirl generator designed by Štefan was used. The base case was simulated using both the RSM and SBES turbulence models. Irregular vortex rope behavior was observed. Two distinct states were detected. The same behavior was observed in recordings from a high speed camera.

A total of 11 installations for mitigating the vortex rope were gradually proposed and tested. The results of CFD simulations with the RSM model of turbulence and/or experiments are presented in Fig. 3.7.

Overall, it can be stated that introducing fins of proper size that deflect the tangential flow in the radial direction, which consequently leads after meeting at the axis to a deflection in the axial direction, stabilize the flow downstream. However, vortices forming at the spike upstream persist and exert periodic load on the fins. It may be therefore reasonable to introduce a kind of active flow control, e.g. water jet injection, to suppress these. On the contrary to the previous section, where the water jet injection was used alone to mitigate the vortex rope and high flow rates were needed, much smaller flow rates should be sufficient since the vortices are substantially weaker.

CFD RSM

CFD SBES

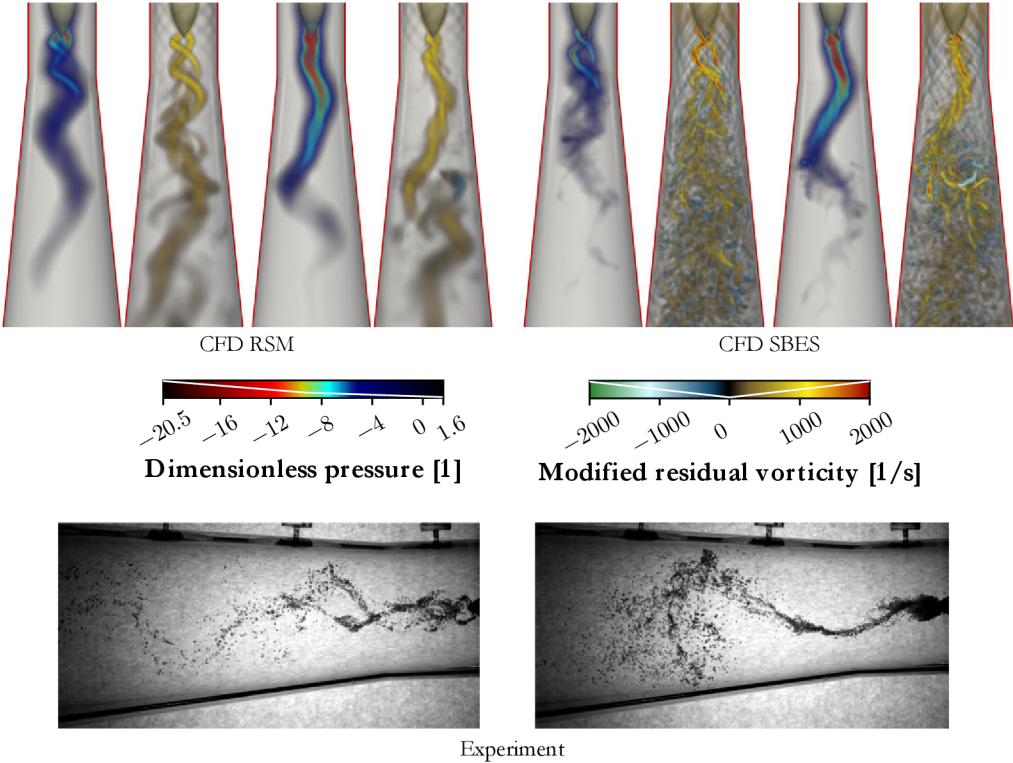Dimensionless pressure [1]

Modified residual vorticity [1/s]

Experiment

Fig. 3.6: *Volume renders of CFD data and photographs from experiment for the base case (without any installation).*

CFD RSM

Dimensionless pressure [1]
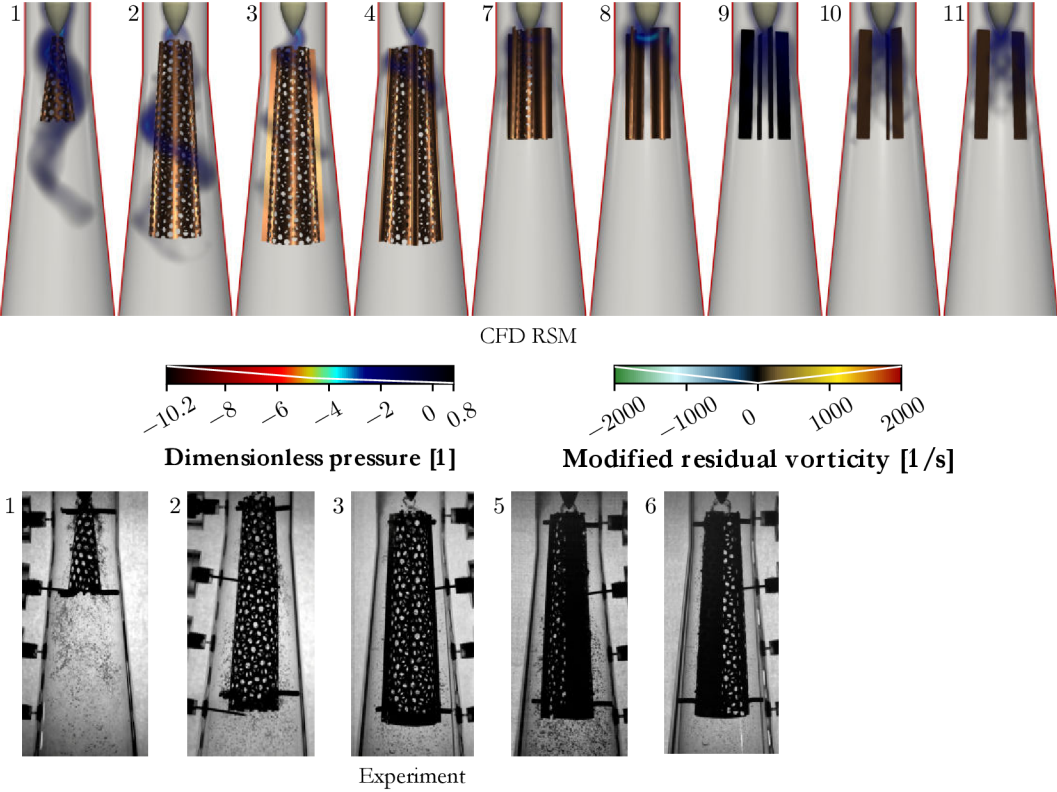
Modified residual vorticity [1/s]

Experiment

Fig. 3.7: *Volume renders of CFD data and photographs from experiments for the cases with installations.*

4 Reduced-order modelling

By reduced-order modelling we mean efforts to reduce computational complexity by decreasing the number of degrees of freedom. To achieve this, we need to find a suitable transformation of coordinates.

To reduce the number of degrees of freedom, the variables shall be formulated in different coordinates, e.g. $p(\boldsymbol{\phi}(\boldsymbol{x}), \boldsymbol{a}(t))$. In this setting, $\boldsymbol{\phi}(\boldsymbol{x})$ is a vector of spatial modes and $\boldsymbol{a}(t)$ a vector of temporal functions governing their evolution. The definition of $p(\boldsymbol{\phi}(\boldsymbol{x}), \boldsymbol{a}(t))$ is then assumed as follows

$$p\big(\boldsymbol{\phi}(\boldsymbol{x}), \boldsymbol{a}(t)\big) = \sum_{i=1}^{m} \phi_i(\boldsymbol{x}) a_i(t) \tag{4.1}$$

4.1 Proper orthogonal decomposition

Given reference data $p(\boldsymbol{x}, t)$, the proper orthogonal decomposition (POD) aims to find spatial and temporal modes satisfying (4.1) and the following condition

$$\iint\limits_{VT} \left(p - p_{\mathrm{POD}}^{[n]}\right)^2 \mathrm{d}V\mathrm{d}t \leq \iint\limits_{VT} \left(p - p_{\mathrm{arb}}^{[n]}\right)^2 \mathrm{d}V\mathrm{d}t \tag{4.2}$$

Here, $p_{\mathrm{POD}}^{[n]}$ is the approximation of p obtained by summing $m = n$ most dominant POD modes in (4.1), and $p_{\mathrm{arb}}^{[n]}$ means the same for $m = n$ arbitrary modes. This condition means that there is no better decomposition than POD in terms of minimizing the square of residual for any given number of modes. Consequently, POD has become very popular for model order reduction.

4.2 Application of POD to the present case

POD will be applied to the data from simulation SBES-T-1, i.e. the simulation with transient boundary conditions covering a range of operating conditions with a well-developed vortex rope. The algorithm will be modified so that it takes into account some characteristic aspects of this transient. The first thing to keep in mind is related to the mean field. It depends on the operating point. Therefore, if the standard POD procedure is applied to the transient case, there will be a mode that covers its evolution. Another aspect is caused by the fact that the vortex rope gets stronger as the swirl number is increased during the transient simulations. The POD optimality condition then causes that the accuracy of reconstructions is significantly biased towards the later phase with much stronger fluctuations. To obtain a balanced performance, a suitable scaling needs to be employed.

The following algorithm was proposed in this work to address the aforementioned aspects.

1) Compute the temporal mean, subtract it from the data, and apply POD the standard way to the obtained fluctuations.
2) Find the POD mode related to the mean field evolution in time. The temporal function of this mode can exhibit a certain level of fluctuations superimposed on a smooth slowly

evolving function. In that case, it may be reasonable to approximate the trend by a suitable function, e.g. by a polynomial or exponential, and disregard the fluctuations.

3) Subtract the mean field and its evolution mode found in the previous step from the original data to obtain only fluctuations related to the vortex rope.

4) Normalize each snapshot as follows

$$\hat{\boldsymbol{p}}'_{i\,\mathrm{norm}} = \frac{\hat{\boldsymbol{p}}'_i}{\sqrt{(\hat{\boldsymbol{p}}'_i, \hat{\boldsymbol{p}}'_i)_V}} \tag{4.3}$$

The result of this step is that the values on the main diagonal of the covariance matrix are the same; therefore, all the snapshots have equal weight in the POD optimality condition.

5) Perform POD of the normalized data set to obtain the spatial modes $\boldsymbol{\phi}_i$.

6) Giving the data of the fluctuations before normalization $\hat{\boldsymbol{p}}'_i$, compute the temporal modes as follows

$$a_i(t_j) = (\boldsymbol{\phi}_i, \hat{\boldsymbol{p}}'_j)_V \tag{4.4}$$

The final results are presented in Fig. 4.1. Mode number 1 is the mean field variation mode. Values of λ and $\lambda_{\mathrm{c}}(m)$ were computed only for the following modes so that only the fast dynamics related to the vortex rope motion are considered. Moreover, values of $\lambda_{\mathrm{c}}(m)$ were computed not only for the whole time interval, but also for its thirds. This reveals the cumulative accuracy of the decomposition in various phases of the vortex rope evolution.

Looking at the pictures of three chosen snapshots and their reconstructions from different number of POD modes, we see that the first eleven modes provide a fairly good approximation of the last snapshot, where a large strong vortex rope is present. Obviously, the smaller structures of which the whole structure is formed are missing, but its shape and pressure decrease towards the center are well captured. In the first two snapshots, we see that the tail of the vortex rope is very blurred. A total of 35 modes need to be taken to obtain the correct shape and many more to achieve the correct pressure values at the centerline. This fact underlines its irregular behavior.

4.3 Methods for predicting unknown states

Intrusive modelling

Intrusive modelling relies on the knowledge of the governing equations. A standard method in POD-based reduced-order modelling is to project the spatial modes onto the governing partial differential equation using the Galerkin projection to obtain a set of ordinary differential equations for temporal modes that can be written as $\dot{\boldsymbol{a}} = f(\boldsymbol{a})$. Lee and Carlberg have recently proposed a generalization of this method for nonlinear modes that can be obtained by a deep autoencoder[9]. However, it was shown by Noack et al.[10] that the standard Galerkin system is often structurally unstable. They showed that for laminar Kármán vortex street (periodic vortex shedding behind a cylinder) close to the onset point, it can be stabilized by incorporating a mode they called the shift mode. This mode is defined as the difference between the temporal mean and the unstable steady solution. The resultant model can predict the development of the instability, i.e. how the

flow transitions from the unstable steady solution to the periodic vortex shedding. Another difficulty comes into play when the residual of the low-dimensional approximation is not negligible. In that case, the effect of the neglected modes needs to be modelled, which is analogous to the closure problem of RANS and LES turbulence modelling[11].
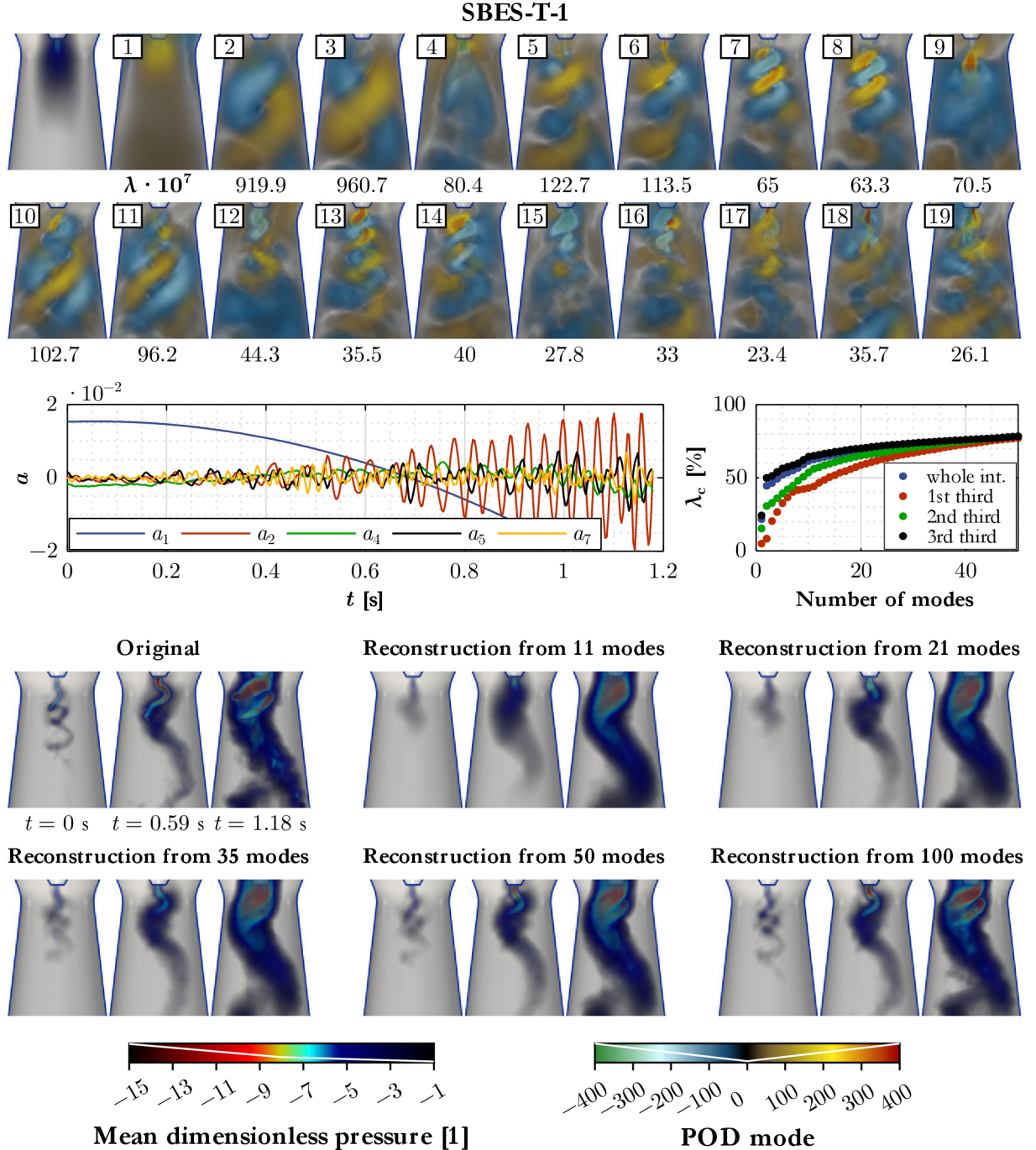

Fig. 4.1: *Results of POD applied to the data from simulation SBES-T-1. Values of λ_c presented in the chart assume only modes from number 2 on, i.e. only the dynamics related to the vortex rope motion. The time interval was divided into thirds to assess the performance of POD in different phases, not just the whole interval.*

Nonintrusive modelling

Nonintrusive modelling is based purely on the input data. Simply said, the task is to find patterns and capture trends in observations of the system. There are cases for which the data are available, but the governing equations are not known or only partially known, e.g. spreading of diseases or brain activity monitoring. In that situations, nonintrusive modelling is essential. Due to the abovementioned difficulties with intrusive modelling, nonintrusive modelling is often utilized also in cases with known governing equations. Thanks to the renewed interest in machine learning in recent years, new techniques have started emerging.

Many approaches revolve around predicting the future evolution of the temporal POD modes $\boldsymbol{a}_i$ or autoencoder latent variables $\boldsymbol{z}$. When it comes to solving various forecasting problems or series processing in general by neural networks, recurrent architectures are typically used. The most prominent of them, the LSTM (Long Short-Term Memory) network, was used by Hasegawa et al.[12] in combination with a convolutional autoencoder to predict the dynamics of a 2D Kármán vortex street. In favorable conditions, the model provided very accurate predictions.

San et al.[13] proposed an architecture of a dense network to advance temporal POD modes in time. Other architectures were proposed by Pawar et al.[14] They also found out that their nonintrusive model substantially outperformed a corresponding intrusive Galerkin model.

4.4 Proposal of a method for quasiperiodic systems

The approach that will be pursued is targeted at the quasiperiodic nature of the most dominant modes. The term quasiperiodicity is defined only loosely. For the purposes of this work, it means that the evolution can be described by a periodic function with parameters that may vary in time to some extent. The following expression is assumed

$$g(t) = (a_0 + a'(t))[\sin(2\pi f_0(t + t'(t)) + \varphi_0)] \tag{4.5}$$

This is in fact a sine function with initial phase φ_0, amplitude $a(t) = a_0 + a'(t)$ varying in time, and frequency varying in time as well, which is modelled by admitting fluctuations of time $t'(t)$. If the frequency evolution in time $f(t) = f_0 + f'(t)$ is known, the following relation for $t'(t)$ can be derived

$$t'(t) = \frac{1}{f_0} \int_0^t f'(t)\,\mathrm{d}t \tag{4.6}$$

In the following, an algorithm for regression of quasiperiodic functions defined above will be proposed. It will be explained on example. Consider a function in the form (4.5), where $a_0 = 1$, $f_0 = 20$, $\varphi_0 = \pi/4$, and

$$a'(t) = \sum_{i=1}^3 a_{i(\mathrm{a}')} \sin\left(2\pi f_{i(\mathrm{a}')} t + \varphi_{i(\mathrm{a}')}\right) \tag{4.7}$$

$$t'(t) = \sum_{i=1}^3 a_{i(t')} \sin\left(2\pi f_{i(t')} t + \varphi_{i(t')}\right) \tag{4.8}$$

Values of the remaining constants are given in the table below.

Tab 4.1: *Values of the constants in the function introduced above.*

i	$a_{i(\mathbf{a}')}$	$f_{i(\mathbf{a}')}$	$\varphi_{i(\mathbf{a}')}$	$a_{i(t')}$	$f_{i(t')}$	$\varphi_{i(t')}$
1	0.01	0.8	0	0.015	1	0
2	0.004	0.5	$\pi/2$	0.005	0.5	0
3	0.002	1.8	$\pi/2$	0.002	2	0

Fluctuations of amplitude and time are therefore expressed as a Fourier series with three components. The constants were chosen so that a moderate modulation of the carrier sine function is obtained. The function in time domain as well as its frequency spectrum for signal length $T = 5$ is plotted below in Fig. 4.2. It turns out that the Fourier transform is in this case misleading since the most dominant peak belongs to $f = 19.2$, while $f_0 = 20$. There are also many other frequencies with nonzero amplitudes on both sides of the most dominant peak. This is caused by the frequency and amplitude modulations since both frequency and amplitude modulation of a carrier signal of frequency f_0 with a modulation signal of frequency f_{m} result in presence of peaks spaced by f_{m} on both sides of the carrier frequency f_0.
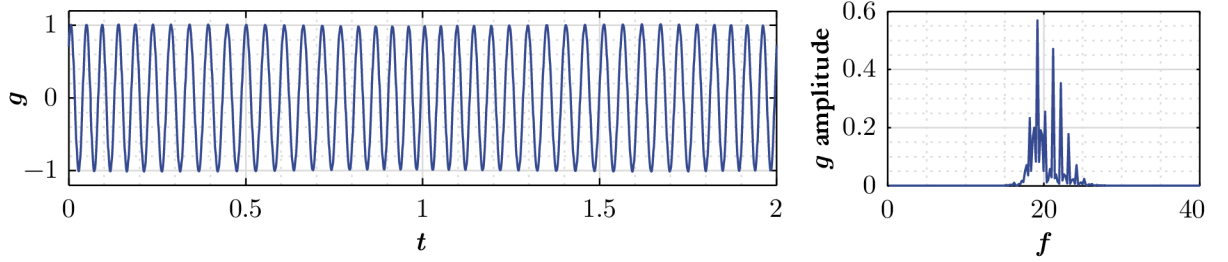

Fig. 4.2: *A plot of the function defined above and its frequency spectrum for signal length $T = 5$.*

Similar situation was observed in the frequency spectra of flow in the present swirl generator. There is no single-frequency peak but rather a certain range of frequencies with higher amplitudes around a dominant frequency, indicating presence of frequency and amplitude fluctuations. Identification of these fluctuations is therefore of interest.

Consider a discrete data set covering the given function $g(t)$ from $t = 0$ to $t = 5$. Assume that the data can be expressed by the form given by (4.5), (4.7), (4.8), which is in this case obviously true. The task is to find the constants in the expressions so that the best fit is obtained. Fitting the constants directly by a fast gradient descend method requiers a very precise initial condition. The following method is proposed to obtain it.

The first step is performing the discrete Fourier transform of the whole signal to detect the dominant frequency, which is in this case $f = 19.2$. Then, data covering the first period T only are taken and the best fit of the following sine function is sought

$$\tilde{g}(a, f, \varphi, t) = a \sin(2\pi f t + \varphi) \tag{4.9}$$

where a, f, and φ need to be determined by minimizing a chosen loss function measuring the difference between the original and the fitted signal. As the initial values of a, f, and φ, the values obtained from the Fourier transform were used. As soon as the best fitting values are obtained, the subsequent period is extracted. The process is repeated until the whole data are processed. The

reason for learning period by period is that the time range needs to be short enough to ensure convergence of gradient-based methods. At the same time, it needs to be long enough for the problem to be well-posed.

After the fitting, the initial values of f_0 and a_0 are computed as the temporal mean of f and a, respectively. The initial phase φ_0 is the phase of the first period. Then, the fluctuating parts $f'(t)$ and $a'(t)$ are computed. By converting $f'(t)$ to $t'(t)$ using (4.6) and applying the Fourier transform to it and $a'(t)$, we can determine the initial values of the constants in (4.7), (4.8). The results of learning are plotted in Fig. 4.3.
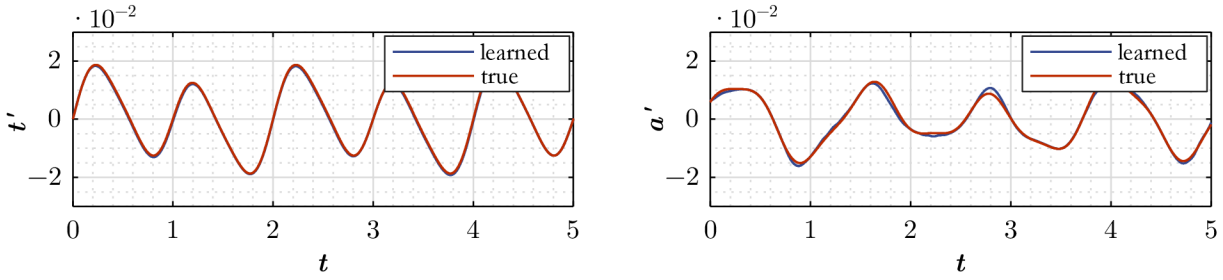

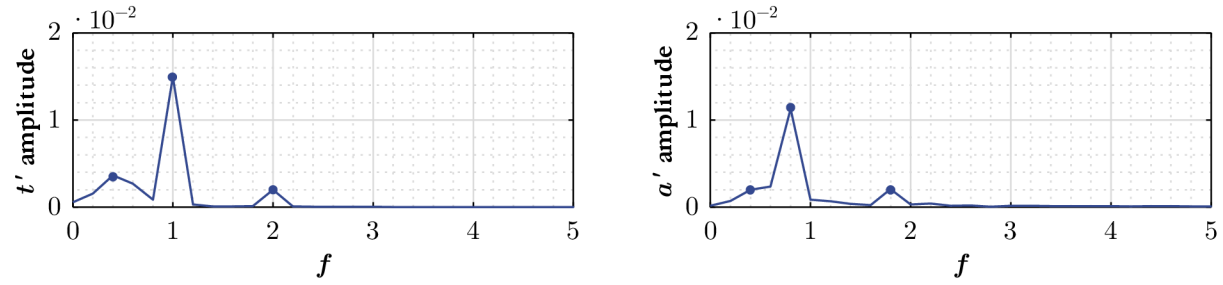**Fig. 4.3:** *Plots of the true and learned fluctuations of time and amplitude.*

Fig. 4.4: *Plots of the frequency spectra of the learned fluctuations of time and amplitude. The designated points will be used as the initial condition in the subsequent learning.*

The results of the Fourier transform are presented in Fig. 4.4. Three most significant points will be used as the initial values of the constants in (4.7), (4.8). The resulting points are designated in the charts. Comparing them with the true values in Tab. 4.1, we see that values for $i = 1$ and 3 agree almost perfectly, whereas the last point, where the true $f = 0.5$ for both time and amplitude fluctuations, is subject to the spectral leakage problem. Knowing initial values of all the constants, it is possible to evaluate the initial condition for the final regression of (4.5), (4.7), (4.8). It is plotted against the true evolution in Fig. 4.5 (left). Only a slight frequency shift is visible. After the final regression, the obtained evolution agrees with the ground truth almost perfectly. By comparing the constants with the true values, it was found out that only one of the less significant components of $a'(t)$ is different (namely that with $f = 0.5$, where the learned value is 0.424, amplitude is slightly lower, and phase is different). The error in the remaining constants is within the desired precision.
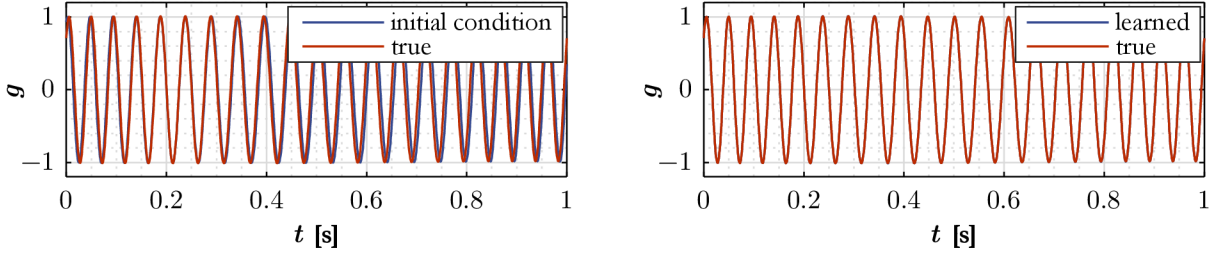
Fig. 4.5: *Left: initial condition for the final fitting in comparison with the true evolution, right: the final result in comparison with the true evolution.*

4.5 Reduced-order model of the present flow with a vortex rope

The method presented in section 4.4 will now be applied to the present case with a vortex rope. The idea is to use the spatial POD modes from the simulation with transient boundary conditions covering a range of operating conditions with a well-developed vortex rope (SBES-T-1, Fig. 4.1). By projecting these modes on the data from simulations with fixed boundary conditions (flow rates ratios 50:50, 60:40, and 70:30), we obtain temporal functions for each regime. The final step is the application of the proposed method to obtain closed-form expressions. Then, the method for identification of quasiperiodic functions was applied to modes with $i \geq 2$. A total of 5 Fourier components were considered for the fluctuations of amplitude and time given by (4.7), (4.8). The temporal function of the first mode (a_1) was assumed constant. It is defined as the mean value of the discrete values $\boldsymbol{a}_1$. Several constraints and measures were considered for the remaining modes in order to enforce known relations and reduce overfitting.

The resultant temporal functions a_2, a_7, and a_{10} are plotted for $t \in \langle 0,3 \rangle$ in Fig. 4.6. It can be observed that the best results were achieved for modes a_2 and a_{10} for the last two regimes, where the quasiperiodicity assumption is justified. On the contrary, mode a_7 has complicated evolutions that are far from periodic. There is a significant discrepancy between the model and the training data; however, the model has learned some of the patterns that can be seen in the training data and repeats them along the way.

Reconstructions of the dimensionless pressure field are presented in Fig. 4.7. Three snapshots from the training range are compared against the original data, and three predictions of the future states are also given to check whether the vortex rope shapes look reasonably. It turned out that most of the reconstructions look credible. Only the snapshots for $t = 0.6$ s and $t = 3$ s for the flow rates ratio of 60:40 exhibit certain phase mismatch between the modes modelling the tail and the upper vortex. Uncoupled nature is therefore the weakest aspect of the present model.

The last step in the development of the reduced-order model is interpolating or aproximating the dependence of the parameters on the operating points. Since only three points were available in this case, an interpolation by a quadratic function was performed. Knowing the dependence of the parameters on the operating point, it was possible to perform reconstructions of the dimensionless pressure fields for operating points covering the range of the flow rates ratio from 50:50 to 70:30. The results are depicted in Fig. 4.8. The value of time t was set to 1 s. It can be seen that the transition is not monotonous. Various forms can be observed on the way from the small weak vortex rope at the beginning to the large strong vortex rope at the end, which agrees with the observations of the transient process in the results of the simulation with transient boundary conditions (SBES-T-1).
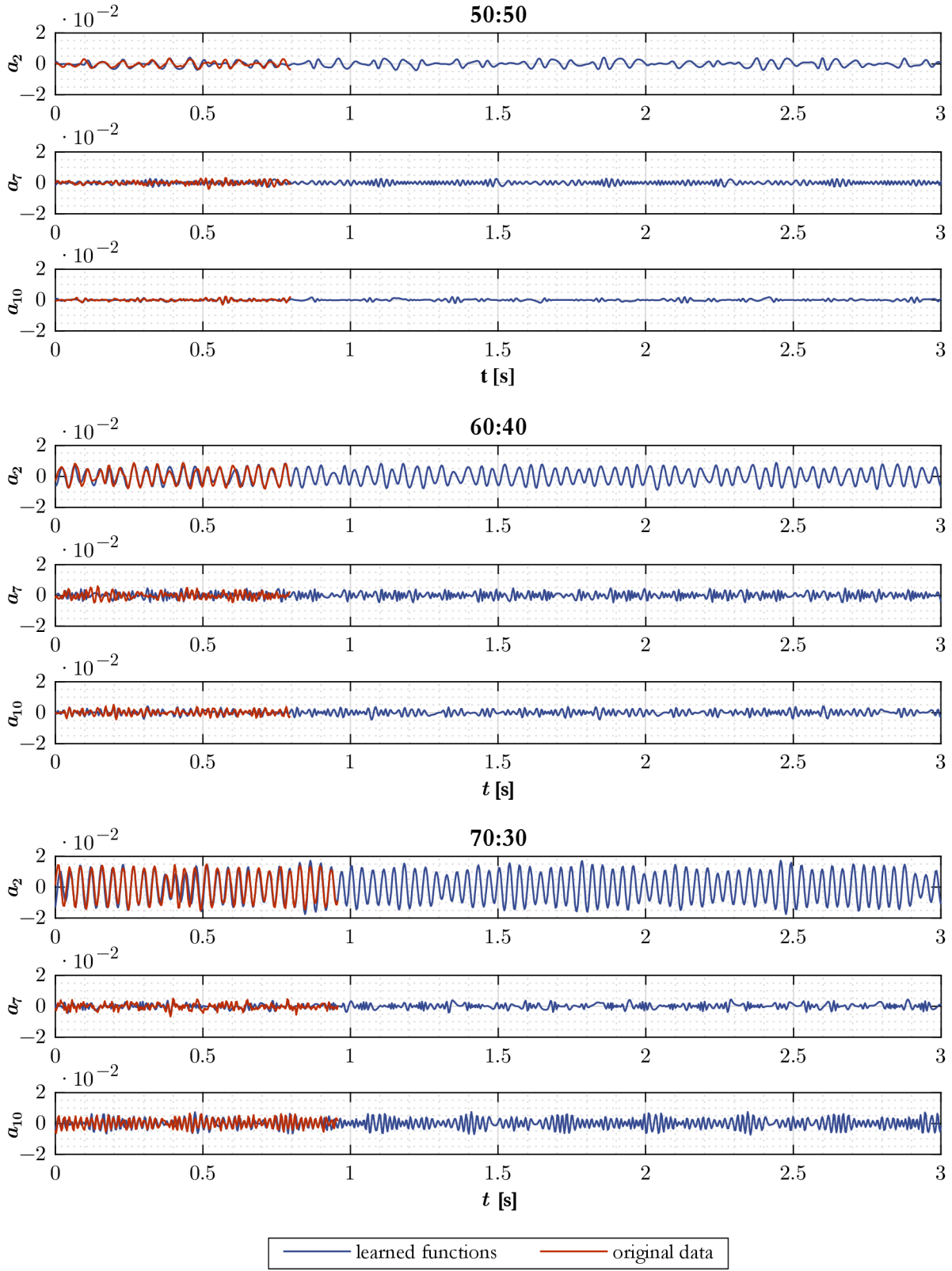
Fig. 4.6: *Original data and learned evolutions of chosen temporal modes of the dimensionless pressure for different operating points.*

50:50

Original — $t = 0$ s $t = 0.3$ s $t = 0.6$ s

Model with 11 modes — $t = 0$ s $t = 0.3$ s $t = 0.6$ s

Model extrapolation — $t = 1$ s $t = 3$ s $t = 20$ s

60:40

Original — $t = 0$ s $t = 0.3$ s $t = 0.6$ s

Model with 11 modes — $t = 0$ s $t = 0.3$ s $t = 0.6$ s

Model extrapolation — $t = 1$ s $t = 3$ s $t = 20$ s

70:30

Original — $t = 0$ s $t = 0.3$ s $t = 0.6$ s

Model with 11 modes — $t = 0$ s $t = 0.3$ s $t = 0.6$ s

Model extrapolation — $t = 1$ s $t = 3$ s $t = 20$ s
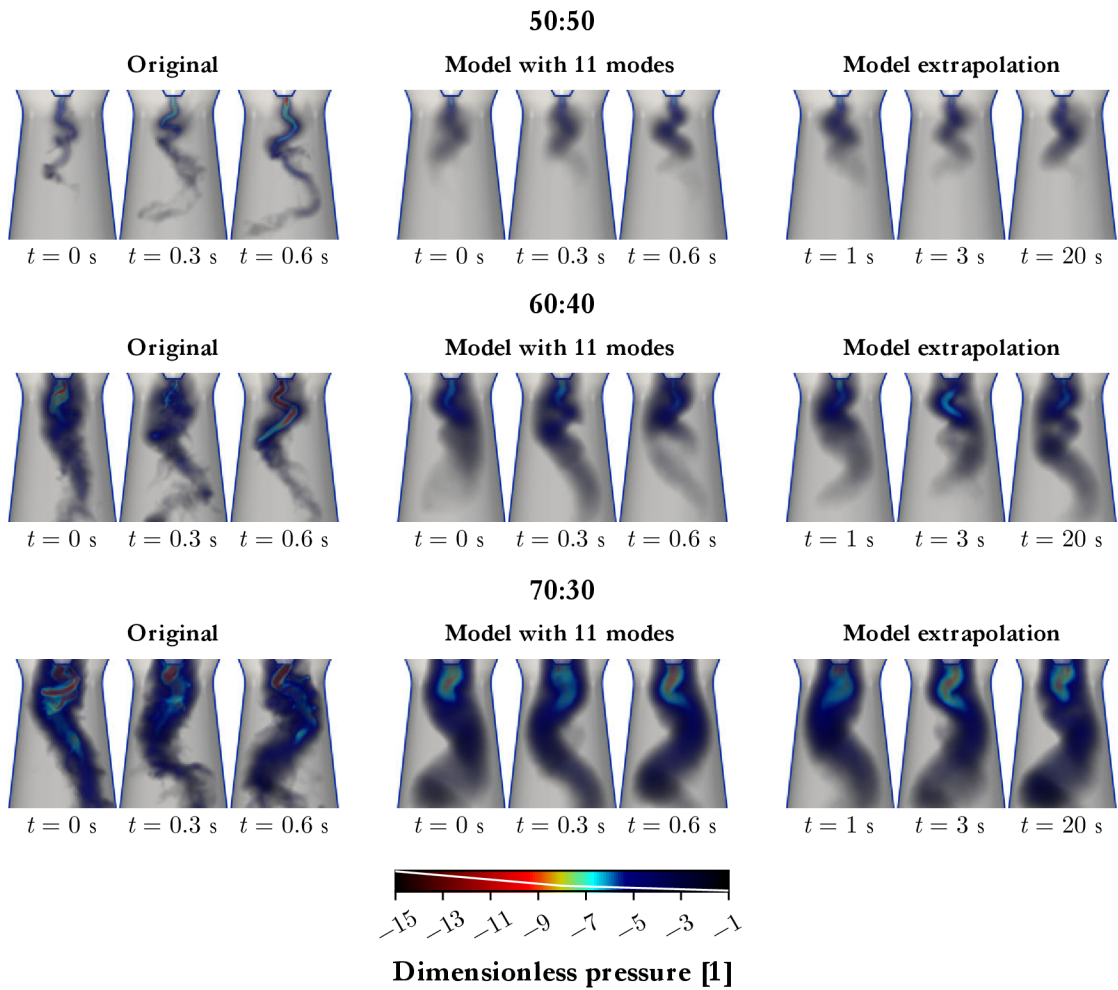
Dimensionless pressure [1]

Fig. 4.7: *Three original snapshots, their approximations from 11 modes identified by machine learning, and extrapolations of the model to the future.*

50:50   51:49   52:48   53:47   54:46   55:45   56:44   57:43   58:42   59:41

60:40   61:39   62:38   63:37   64:36   65:35   66:34   67:33   68:32   69:31
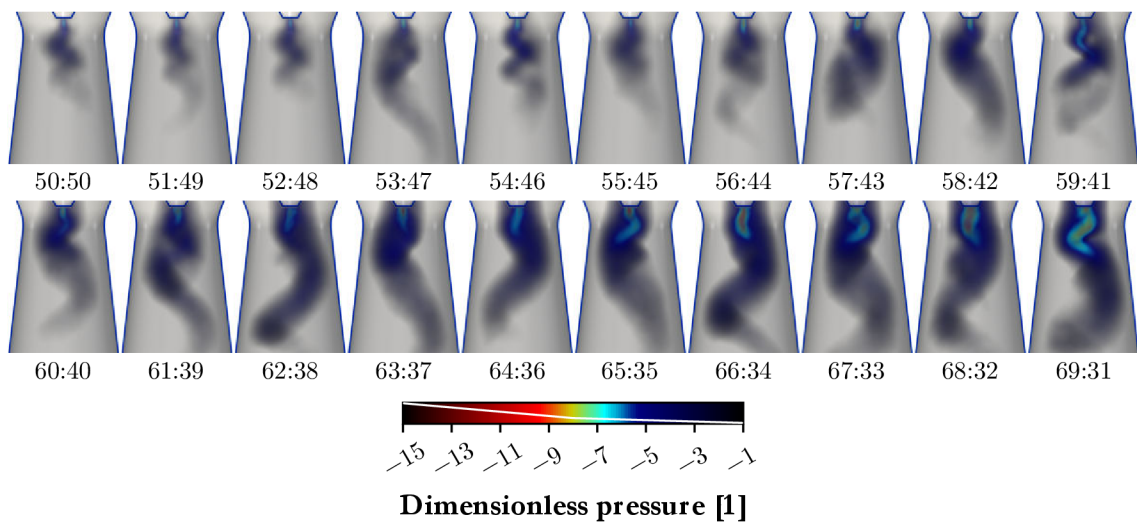
Dimensionless pressure [1]

Fig. 4.8: *Reconstructions of the dimensionless pressure field for the same time instant and various flow rates ratios listed below each picture.*

Conclusions

The present work dealt with the vortex rope phenomenon. It is a comprehensive study describing the whole process from designing a new swirl generator through CFD study of the flow to proposing reduced-ordel modelling methods. It resulted in many findings that will now be summarized. Also, several ideas were given but not elaborated within this work. They are therefore left as suggestions for future research.

The newly designed swirl generator fills the gap between precise but expensive devices and cheap devices without any regulation of the swirl intensity.

Many CFD simulations with the SBES model of turbulence have been performed. The CFD results were verified by comparison with the PIV measurements. The evolution of the vortex rope with increasing swirl intensity was thoroughly studied. For this purpose, visualization methods based on volume rendering have been devised, and many criteria for the detection of vortical structures have been tested. The residual vorticity was found to provide the best results in vortex identification and therefore became the method of choice in this work.

A brief study of both active and passive methods to mitigate the vortex rope has also been carried out. A cautionary outcome is that if water jet injection through the hub tip is applied, the jet may start rotating around the diffuser axis due to the circumferential velocity of the outer swirling flow, eventually causing stronger pressure pulsations than uncontrolled vortex rope itself. The best results were achieved for water jet injection through a greater cross section. It suggests that a sufficiently high diameter of the jet is needed to prevent the mentioned undesired behavior. Unfortunately, the method is still energetically costly. Several passive methods were studied using a different swirl generator. It turned out that fins of proper size and position may stabilize the flow downstream. However, vortical structures persist upstream and exert an unsteady load on the fins. Therefore, it may be reasonable to use an active flow control method to suppress these vortices.

The last part was dedicated to reduced-order modelling. In this work, a nonintrusive technique aimed at the identification of quasiperiodic patterns in the temporal functions has been proposed. It resides in choosing a suitable expression for the POD temporal functions and finding the parameters by machine learning. This task is complicated by the fact that the loss function is oscillatory; therefore, fast algorithms based on gradient descent need a good initial condition in order to avoid getting stuck in an unfavorable local minimum. For that reason, a method for determining a good initial condition has been proposed. It works well for functions satisfying the quasiperiodicity assumptions. For more complex functions, the performance is obviously poorer, and the model gets prone to overfitting.

In the present case, it turned out that the quasiperiodicity assumptions hold well for the most dominant mode pair at operating points with a higher swirl intensity. This mode pair is related to the precessing motion of the vortex rope tail. In fact, the spatial modes correspond to its mean shape. The model can be used to quantify variations in the frequency and amplitude of the pressure pulsations caused by this leading-mode pair. Interpolation between operating points led to credible results, i.e. the model is able to capture the trend.

The temporal functions of other modes were far from the quasiperiodicity assumptions. Several measures for aiding the model generalizability were used, including matching the frequency spectra after extrapolation to the future with those of the training data within the loss function and enforcing known phase shifts for the paired modes. Still, the model works more as a generator of functions that satisfy these constraints rather than reliably identifying trends in the data. Nevertheless, reconstructions of the pressure field look good. The patterns observed in the training data are preserved; only sometimes a phase mismatch can be observed between parts of the vortex rope.

References

[1] JUNGINGER, B. and S. RIEDELBAUCH. Analysis of a full load operating point of a propeller turbine using scale-resolving turbulence models. *WASSERWIRTSCHAFT*. 2019, **109**(S1), 124–129. DOI: 10.1007/s35147-019-0248-7. ISSN 0043-0978.

[2] URBAN, O., M. KURKOVÁ and P. RUDOLF. Application of Computer Graphics Flow Visualization Methods in Vortex Rope Investigations. *Energies*. 2021, **14**(3), 623. DOI: 10.3390/en14030623. ISSN: 1996-1073.

[3] ČASTULÍKOVÁ, V. *Metody počítačové vizualizace proudění*. Brno, 2019. Bachelor's thesis. Brno University of Technology. Supervisor O. Urban.

[4] KURKOVÁ, M. *Studium vírových struktur vznikajících ve vírovém generátoru*. Brno, 2020. Bachelor's thesis. Brno University of Technology. Supervisor O. Urban.

[5] KAUFMAN, A., K. HÖHNE, W. KRÜGER, L: ROSENBLUM and P. SCHRÖDER. Research issues in volume visualization. *IEEE Computer Graphics and Applications*. 1994, **14**(2), 63–67. DOI: 10.1109/38.267473. ISSN: 0272-1716.

[6] ROSENBLUM, L. J. Research issues in scientific visualization. *IEEE Computer Graphics and Applications*. 1994, **14**(2), 61–63. DOI: 10.1109/38.267472. ISSN: 0272-1716.

[7] KOLÁŘ, V. Vortex identification: New requirements and limitations. *International Journal of Heat and Fluid Flow*. 2007, **28**(4), 638–652. DOI: 10.1016/j.ijheatfluidflow.2007.03.004. ISSN 0142-727X.

[8] URBAN, O., M. KURKOVÁ and F. POCHYLÝ. *Analytický rozbor recirkulace na vstupu do oběžného kola odstředivého čerpadla, posouzení opatření pro její omezení*. Brno, 2021. Research report. Brno University of Technology.

[9] LEE, K. and K. T. CARLBERG. Model reduction of dynamical systems on nonlinear manifolds using deep convolutional autoencoders. *Journal of Computational Physics*. 2020, **404**, 108973. DOI: 10.1016/j.jcp.2019.108973. ISSN 0021-9991.

[10] NOACK, B. R., K: AFANASIEV, M. MORZYŃSKI, G. TADMOR and F. THIELE. A hierarchy of low-dimensional models for the transient and post-transient cylinder wake. *Journal of Fluid Mechanics*. 2003, **497**, 335–363. DOI: 10.1017/S0022112003006694. ISSN 0022-1120.

[11] WANG, Z., I: AKHTAR, J. BORGGAARD and T. ILIESCU. Proper orthogonal decomposition closure models for turbulent flows: A numerical comparison. *Computer Methods in Applied Mechanics and Engineering*. 2012, **237–240**, 10–26. DOI: 10.1016/j.cma.2012.04.015. ISSN 0045-7825.

[12] HASEGAWA, K., K. FUKAMI, T. MURATA and K. FUKAGATA. CNN-LSTM based reduced order modeling of two-dimensional unsteady flows around a circular cylinder at different Reynolds numbers. *Fluid Dynamics Research*. 2020, **52**(6), 065501. DOI: 10.1088/1873-7005/abb91d. ISSN 1873-7005.

[13] SAN, O., R. MAULIK and M. AHMED. An artifical neural network framework for reduced order modeling of transient flows. *Communications in Nonlinear Science and Numerical Simulation*. 2019, **77**, 271–287. DOI: 10.1016/j.cnsns.2019.04.025. ISSN 1007-5704.

[14] PAWAR, S., S. M. RAHMAN, H. VADDIREDDY, O. SAN, A. RASHEED and P. VEDULA. A deep learning enabler for nonintrusive reduced order modeling of fluid flows. *Physics of Fluids*. 2019, **31**, 085101. DOI: 10.1063/1.5113494. ISSN 1070-6631.

Author's CV

Name: Ondřej URBAN
Date and place of birth: 3. 11. 1992, Brno, Czech Republic

Education

2017–2022
Doctoral degree – Design and process engineering, Faculty of Mechanical Engineering, Brno University of Technology. Thesis: Reduced-order model of swirling flow

2015–2017
Master's degree – Fluid engineering, Faculty of Mechanical Engineering, Brno University of Technology. Thesis: Reduced-order model of swirling flow

2012–2015
Bachelor's degree – Fundamentals of mechanical engineering, Faculty of Mechanical Engineering, Brno University of Technology. Thesis: Dancing liquid – vibration eigenmode shapes of liquids

Work experience

2022–present
Researcher – Viktor Kaplan Department of Fluid Engineering, Faculty of Mechanical Engineering, Brno University of Technology

2018–2021
Ph.D. researcher – Viktor Kaplan Department of Fluid Engineering, Faculty of Mechanical Engineering, Brno University of Technology

Abstract

This doctoral thesis is aimed at studying the vortex rope phenomenon. For this purpose, a new swirl generator capable of regulating the swirl intensity was designed. The behavior of the vortex rope was studied both numerically and experimentally. Scale-resolving numerical simulations were employed, visualization methods based on volume rendering were proposed, and different vortex criteria were tested. Several flow field decomposition methods were studied. Finally, methods for extracting quasiperiodic patterns were proposed. These methods enabled the construction of a reduced-order model for a range of operating conditions.